Journal of Composite Materials OnlineFirst, published on September 20, 2005 as doi:10.1177/0021998305057365

Micromechanical Analysis of Composite Laminates at Cryogenic Temperatures

SUKJOO CHOI AND BHAVANI V. SANKAR*
Department of Mechanical and Aerospace Engineering
University of Florida
Gainesville, FL 32611, USA

(Received October 6, 2004)
(Accepted June 4, 2005)

ABSTRACT: A finite element analysis-based micromechanics method is developed to investigate development of microcracks in a graphite/epoxy composite liquid hydrogen tank at cryogenic temperatures. The unit cell of the composite is modeled using finite elements. Periodic boundary conditions are applied to the boundaries of the unit cell. The temperature-dependent properties including the coefficient of thermal expansion of the matrix material are taken into account in the analysis. The thermoelastic constants of the composite are calculated as a function of temperature. The stresses in the fiber and matrix phases and along the fiber–matrix interface are calculated. When the laminated composite structure is subjected to combined thermal and mechanical loads, the macrostrains are computed from the global analysis. Then, the macrostrains and temperatures are applied to the unit cell model to evaluate microstresses, which are used to predict the formation of microcracks in the matrix. The method is applied to a composite liquid hydrogen storage system. It is found that the stresses in the matrix phase could be large enough to cause microcracks in the composite.

KEY WORDS: composite material, cryogenics, graphite/epoxy, liquid hydrogen storage, microcracks, micromechanics, periodic boundary conditions, thermal stresses, unit cell.

INTRODUCTION

THE NEXT GENERATION reusable space launch vehicle is proposed to provide a tenfold reduction in the cost of launching payloads into space, from 10,000 to $1000 per pound. Reducing the structure weight of the vehicle is of paramount importance in reducing the launch cost. Composite materials such as graphite/epoxy offer many advantages, such as low density, high specific stiffness and specific strength, and low coefficient of thermal expansion (CTE). Therefore, fiber composite materials are

*Author to whom correspondence should be addressed. E-mail: sankar@ufl.edu

0021-9983/05/00 0001–15 $10.00/0 DOI: 10.1177/0021998305057365

candidate materials for cryogenic storage tanks for liquid hydrogen. In this article, we study the problems in using fiber-reinforced composites at cryogenic temperatures as occurs in composite tanks used for storing liquid hydrogen (LH2).

When the LH2 composite tank is subjected to combined thermal and mechanical loads, microcracks develop in the fiber composite, which cause permeation of hydrogen through the microcracks [1]. This can lead to very dangerous conditions in the vehicle including catastrophic failure. From a macroscopic perspective, the composite material is considered to be homogeneous and transversely isotropic or in general, orthotropic. For example, the laminated plate theory has been formulated based on this assumption. Even when three-dimensional analyses are used for composite structures, each ply or layer of the composite is modeled as a homogeneous orthotropic material. This macroscopic approximation has been found to be satisfactory in most situations including thermal stress analyses. Thus most of the thermal stress problems in composites focus on the differences in thermal expansion coefficients between the plies. However, in extreme situations a micromechanics approach wherein the fiber and matrix phases are differentiated is necessary for accurate prediction of stresses, and hence failure. The present problem falls in this category. To predict the failure of a composite structure at macroscopic scale, an investigation of the micromechanical behavior is necessary to understand the failure mechanisms in the fibers and matrix at a microscale [2].

Before finite element (FE) methods were widely available, micromechanics analysis of fiber-reinforced composites was performed using analytical methods, for example, Chen and Cheng [3]. They analyzed the unit cell of a composite by solving the governing elasticity equations using an infinite series and employing a combination of Fourier series and least square methods. The periodic boundary conditions for stresses and displacements were satisfied on symmetric boundaries. Micromechanics analysis methods for elastic-plastic composites were investigated using the bounding technique by Teply and Dvorak [4]. The problem of elastic-viscoplastic composites was solved by imposing continuity of traction and displacement rate at the interfaces between the constituents of a square unit cell by Paley and Aboudi [5]. A square unit cell model was used to investigate the behavior of fiber-reinforced composites subjected to shear loading by Nedele and Wisnom [6]. Marrey and Sankar [7–9] developed micromechanics methods for textile structure composites using the FE method. Their method considered the effects of stress gradients on the strength and stiffness properties of the composite.

In the present study, the micromechanics method is combined with a global laminate analysis to predict the stresses in the fiber and matrix phases accurately. The method is used to predict the development of microcracks in a composite laminate at cryogenic temperatures. To predict the development of microcracks in fiber composites, one needs accurate description of the stresses in the matrix phase and also along the fiber–matrix interface. The problem of thermal stresses is complicated by the temperature-dependent properties of the constituent materials. In the present study, a global/local approach is used wherein traditional structural analysis is used to obtain information on macrostrains in a ply in the composite laminate. Then the macrostrains along with the local temperature are used in a micromechanical analysis to obtain detailed information on the stresses in the constituent phases. Two types of representative volume elements (RVEs) are used in the micromechanical analyses. In the first one, the RVE is a square with a circular fiber at the center of the square. In the second, a hexagonal RVE is used. The differences in thermal stresses in the two RVEs are discussed. The temperature dependence of the matrix CTE is taken into account in the micromechanics. The microstresses in different types

of laminates used in a typical LH2 tank are studied and the possibility of microcracking is discussed. The results indicate that the maximum tensile stresses in the brittle matrix reach values very close to the tensile strength of the matrix material raising the possibility of microcrack development in composite liquid hydrogen storage systems.

MICROMECHANICAL MODEL

The microscopic image of a uniaxial fiber-reinforced laminate (Figures 1 and 2) shows that the fiber arrangement is quite random in reality. However, for analytical/numerical modeling, it is convenient to assume some repetitive pattern of fiber arrangement. In the present analysis, both square and hexagonal unit cells are considered. In both cases, the dimensions are chosen such that the fiber volume ratio is 60%, which is typical of graphite/epoxy composites. When fibers are arranged in a square unit cell, one can obtain a maximum fiber volume fraction of 79%. The square unit cell was modeled using 1600 quadratic solid elements with periodic boundary conditions [7–9]. The periodic boundary conditions ensure displacement compatibility and stress continuity on the opposite faces of the unit cell.

The hexagonal pattern of unit cell can be found more commonly in fiber–matrix composites, especially when the composite is fabricated with high fiber volume fraction. Theoretically, one can obtain a maximum fiber volume fraction of 91% with hexagonal RVE. In a hexagonal RVE, there is symmetry about the y-axis and also about the $\pm 30^{\circ}$ directions. The hexagonal unit cell is modeled using 2400 quadratic solid elements with periodic boundary conditions [10].

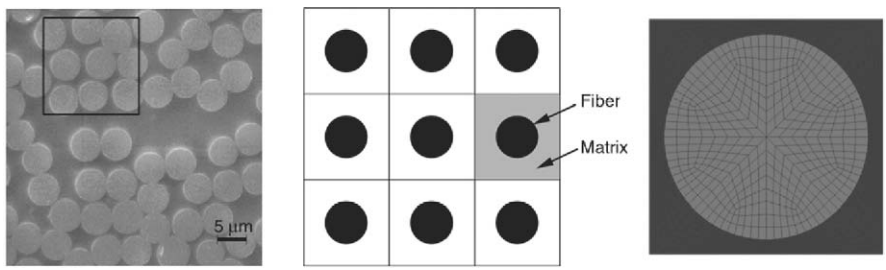

Figure 1. *A square representative volume element and corresponding finite element mesh.*

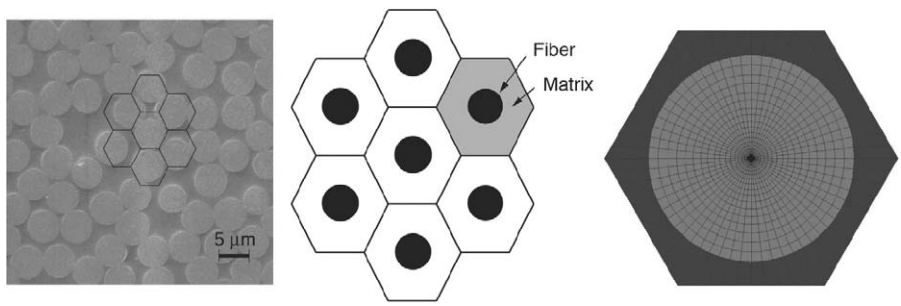

Figure 2. *A hexagonal RVE and corresponding FE mesh.*

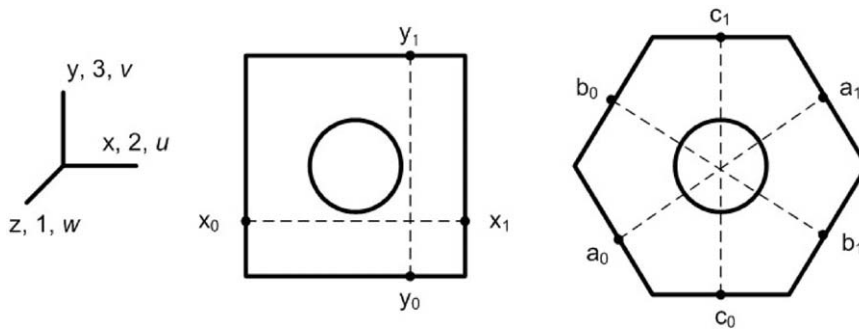

Figure 3. *Geometry of square and hexagonal unit cells.*

Table 1. Periodic boundary conditions for the square unit cell for unit values of different strain components.

$\varepsilon_x = 1$	$\varepsilon_y = 1$	$\varepsilon_z = 1$	$\gamma_{xy} = 1$	$\gamma_{xz} = 1$	$\gamma_{yz} = 1$
$u_{x1} - u_{x0} = L$	$u_{x1} - u_{x0} = 0$	$u_{x1} - u_{x0} = 0$	$v_{x1} - v_{x0} = 0.5L$	$w_{x1} - w_{x0} = L$	$w_{y1} - w_{y0} = L$
$v_{y1} - v_{y0} = 0$	$v_{y1} - v_{y0} = L$	$v_{y1} - v_{y0} = 0$	$u_{y1} - u_{y0} = 0.5L$	$u_{z1} - u_{z0} = 0$	$v_{z1} - v_{z0} = 0$
$w_{z1} - w_{z0} = 0$	$w_{z1} - w_{z0} = 0$	$w_{z1} - w_{z0} = t$	$w_{z1} - w_{z0} = 0$		

Table 2. Periodic boundary conditions for the hexagonal unit cell for unit values of different strain components.

$\varepsilon_x = 1$	$\varepsilon_y = 1$	$\varepsilon_z = 1$	$\gamma_{xy} = 1$	$\gamma_{xz} = 1$	$\gamma_{yz} = 1$
$u_{a1} - u_{a0} = \sqrt{3}/2L$	$u_{a1} - u_{a0} = 0$	$u_{a1} - u_{a0} = 0$	$u_{a1} - u_{a0} = 0$	$u_{z1} - u_{z0} = 0$	$v_{z1} - v_{z0} = 0$
$u_{b1} - u_{b0} = \sqrt{3}/2L$	$u_{b1} - u_{b0} = 0$	$u_{b1} - u_{b0} = 0$	$u_{b1} - u_{b0} = 0$	$u_{c1} = 0$	$w_{c1} = L/2$
$v_{a1} - v_{a0} = 0$	$v_{a1} - v_{a0} = L/2$	$v_{a1} - v_{a0} = 0$	$u_{c1} = 0$	$u_{c0} = 0$	$w_{c0} = -L/2$
$v_{b1} - v_{b0} = 0$	$v_{b1} - v_{b0} = L/2$	$v_{b1} - v_{b0} = 0$	$u_{c0} = 0$	$v_{c1} = 0$	$w_{a1} - w_{a0} = L/2$
$v_{c1} = 0$	$v_{c1} = L/2$	$v_{c1} = 0$	$v_{a1} - v_{a0} = \sqrt{3}/2L$	$v_{c0} = 0$	$w_{b0} - w_{b1} = L/2$
$v_{c0} = 0$	$v_{c0} = -L/2$	$v_{c0} = 0$	$v_{b1} - v_{b0} = -\sqrt{3}/2L$	$w_{a1} - w_{a0} = \sqrt{3}/2L$	
$w_{z1} - w_{z0} = 0$	$w_{z1} - w_{z0} = 0$	$w_{z1} - w_{z0} = t$	$w_{z1} - w_{z0} = 0$	$w_{b1} - w_{b0} = \sqrt{3}/2L$	

The unit cells are subjected to axial and shear displacements combined with thermal effects using periodic boundary conditions. The periodic boundary conditions maintain equal boundary displacements with the adjacent unit cells to satisfy the compatibility of displacements on opposite faces of the unit cell and enforce the continuity of stresses. The unit cell is subjected to different strain components individually using the periodic boundary conditions shown in Table 1 (see Figure 3) [7–9]. For the hexagonal unit cell, the periodic boundary conditions corresponding to unit value of each strain component are shown in Table 2 [10]. The equations of periodic boundary conditions corresponding individual unit strains were embedded in the ABAQUS® input code to perform the FE analysis.

THERMOELASTIC PROPERTIES OF THE COMPOSITE CONSTITUENTS

For accurate prediction of stresses at cryogenic conditions, one requires temperature-dependent thermoelastic properties of the constituent materials. In the present study,

the matrix properties are considered as temperature dependent and the fiber properties as temperature independent. In most of the advanced composite systems such as aerospace graphite/epoxy are cured at about 455 K. When the temperature rises above the melting temperature T_m, the epoxy resin becomes a rubbery solid and then becomes a viscous liquid. When the laminate is cooled down to the glass transition temperature T_g, the epoxy resin becomes an amorphous solid. The difference in the CTEs for the constituents under temperature changes causes residual stresses in the composite laminate. Thermal stresses in composites are largely influenced by matrix thermomechanical properties. Also, the chemical reaction of epoxy causes shrinkage, which rises residual stress in the matrix phase. In this study, the residual stress due to chemical reaction of epoxy is assumed to be negligible.

In this study, the 977-3 epoxy system is used as the matrix material. The CTE and the Young's modulus of this material system [11] as a function of temperature are shown in Figure 4, respectively. The actual and average CTE of the epoxy resin are nonlinear with respect to temperature. The average CTE from a reference temperature is used as input in the ABAQUS® FE program. The average CTE is calculated by using the relation

$$\bar{\alpha} = \frac{\int_{T_{\text{curing}}}^{T_{\text{cryogenic}}} \alpha(T)\,\mathrm{d}T}{T - T_{\text{curing}}} \tag{1}$$

In the above equation, the curing temperature T_{curing} is 455 K where the epoxy resin becomes solid during the curing process of composite laminates. The cryogenic temperature $T_{\text{cryogenic}}$ is 50 K where the liquid hydrogen boils.

When the temperature decreases from curing to cryogenic temperature, the actual CTE decreases from 73.0×10^{-6}/K to 18.1×10^{-6}/K and the Young's moduli increases from 1.2 to 5.2 MPa. The tensile strength for heat-cured epoxy is in the range of 70–90 MPa at room temperature [11]. In general, the strength of epoxy increases from curing to cryogenic temperature since the epoxy becomes brittle [11,12], but no data are available in the complete range of temperatures up to liquid hydrogen temperature. In this study, the tensile strength of the epoxy is assumed as 100 MPa at cryogenic temperature.

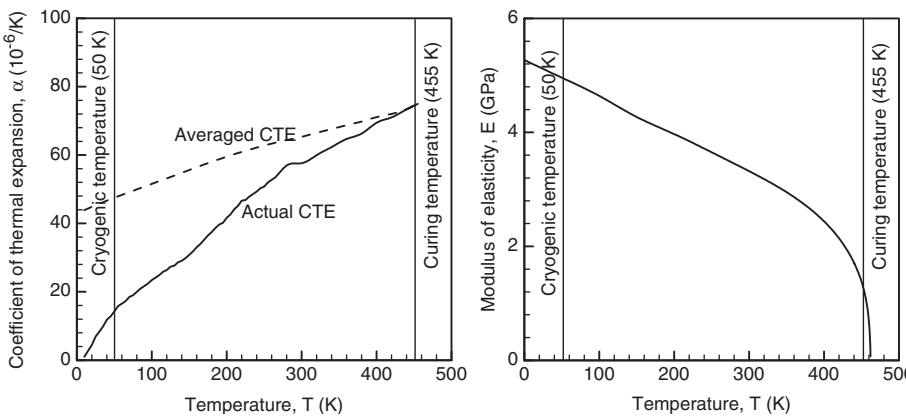

Figure 4. *CTE and Young's modulus of epoxy as a function of temperature.*

Table 3. Material properties of fibers used in the verification problem.

	***E*-glass fiber**	**Graphite fiber (IM7)**
E_1 (GPa)	72.4	263
E_2, E_3 (GPa)	72.4	19
G_{12}, G_{13} (GPa)	30.2	27.6
G_{23} (GPa)	30.2	27.6
ν_{12}, ν_{13}	0.2	0.2
ν_{23}	0.2	0.35
α_{11} (10^{-6}/°C)	5.0	−0.9
α_{22}, α_{33} (10^{-6}/°C)	5.0	7.2
Tensile strength (MPa)	1104	1725

The transversely isotropic properties of the glass and graphite fibers used in this study are shown in Table 3 [13,14]. The material properties of fiber are assumed to be independent of temperature changes.

ESTIMATION OF THERMOELASTIC CONSTANTS

The unit cell model is used to estimate the elastic constants and the CTE using the FE-based micromechanics method. The fiber volume fraction was assumed to be 60%. The thermoelastic stress–strain relations of the composite material at macroscale can be written as:

$$\begin{Bmatrix} \sigma_1 \\ \sigma_2 \\ \sigma_3 \\ \tau_{23} \\ \tau_{31} \\ \tau_{12} \end{Bmatrix} = \begin{bmatrix} C_{11} & C_{12} & C_{13} & 0 & 0 & 0 \\ & C_{22} & C_{23} & 0 & 0 & 0 \\ & & C_{33} & 0 & 0 & 0 \\ & & & C_{44} & 0 & 0 \\ & \text{SYM} & & & C_{55} & 0 \\ & & & & & C_{66} \end{bmatrix} \left\{ \begin{pmatrix} \varepsilon_1 \\ \varepsilon_2 \\ \varepsilon_3 \\ \gamma_{23} \\ \gamma_{31} \\ \gamma_{12} \end{pmatrix} - \Delta T \begin{pmatrix} \alpha_1 \\ \alpha_2 \\ \alpha_3 \\ \alpha_{23} \\ \alpha_{31} \\ \alpha_{12} \end{pmatrix} \right\} \tag{2}$$

The elastic constants and the CTEs in Equation (2) were obtained by performing 7 sets of micromechanical analyses. In the first 6 cases, the temperature difference ΔT was set to zero and the unit cell was subjected to periodic boundary conditions corresponding to one of the macrostrains as given in Tables 1 and 2. The macrostresses in the unit cell were calculated as the volume average of the corresponding microstress components:

$$\sigma_i = \frac{1}{V} \sum_{k=1}^{\text{NELM}} \sigma_i^{(k)} V^{(k)}, \qquad i = 1, 6 \tag{3}$$

In Equation (3), k denotes the element number, NELM is the total number of elements in the FE model, $V^{(k)}$ the volume of the kth element, and V the volume of the unit cell. The average or macrostresses are used to calculate the stiffness coefficients in a column corresponding to the nonzero strain. To calculate the CTEs, the unit cell is subjected to periodic boundary conditions such that the macrostrains are identically equal to zero and

a uniform ΔT is applied to the unit cell. From the macrostresses, the CTEs can be calculated as:

$$\{\alpha\} = \frac{1}{\Delta T}[C]^{-1}\{\sigma\} \tag{4}$$

In this study, the properties and residual stresses were calculated at 50 K, which corresponds to $\Delta T = -405$ K. The elastic constants, such as Young's moduli, shear moduli, and Poisson's ratios can be obtained from the compliance matrix $S = C^{-1}$.

The thermoelastic constants determined from the micromechanical analyses are compared with available empirical formulas in Table 4. Halpin–Tsai [13] equations are used to calculate the approximate elastic constants and Schaprey's formulas [13] are used for the CTEs in Table 4. The results from the FE model and the empirical formulas agree reasonably well. The elastic moduli E_1 and E_2 from the FE models and the empirical formulas differ by less than 4%. However, the transverse modulus is very sensitive to the geometry of the unit cell. Since Halpin–Tsai equations are empirical, the method cannot accurately predict the transverse modulus. There are no simple solutions to estimate the elastic properties G_{23} and v_{23} [13]. In the present study, the properties G_{23} and v_{23} are estimated by the Halpin–Tsai [13] equations and the difference is comparatively larger than the other results.

To verify the transverse isotropy of the square and hexagonal unit cells, the shear modulus G_{23} calculated from the transverse Young's modulus and Poisson's ratio is compared with the G_{23} calculated using the results from the FE analysis. If the composite is truly transversely isotropic, then it should satisfy the relation $G_{23} = (E_2/2(1 + v_{23}))$.

Table 4. Results of elastic constants for glass/epoxy and graphite/epoxy laminates.

			Square unit cell (SQR)		Hexagonal unit cell (HEX)		
	Elastic constants	**Empirical formulas (EMP)**	**FE result**	**Difference between SQR and EMP (%)**	**FE result**	**Difference between HEX and EMP (%)**	**Difference between SQR and HEX (%)**
Glass/ epoxy	E_1 (GPa)	45.4	45.4	0.13	45.5	0.13	0.26
	E_2, E_3 (GPa)	19.4	19.7	2.02	16.3	18.5	17.3
	G_{12}, G_{13} (GPa)	6.00	6.10	1.60	5.59	7.31	8.30
	G_{23} (GPa)	7.71	4.62	66.8	5.83	32.2	26.1
	ν_{12}, ν_{13}	0.260	0.253	2.83	0.260	0.08	2.91
	ν_{23}	0.255	0.275	7.35	0.391	33.1	38.5
	α_{11} (10^{-6}/°C)	5.41	5.45	0.75	5.46	0.91	0.16
	α_{22}, α_{33} (10^{-6}/°C)	9.92	9.04	9.75	9.27	7.03	2.54
Graphite/ epoxy	E_{11} (GPa)	160	159	0.43	160	0.10	0.33
	E_{22}, E_{33} (GPa)	11.1	11.5	3.75	10.8	2.31	5.92
	G_{12}, G_{13} (GPa)	5.90	5.98	1.41	5.50	7.17	8.01
	G_{23} (GPa)	4.05	3.40	19.0	3.72	8.99	9.20
	ν_{12}, ν_{13}	0.260	0.257	1.29	0.254	2.29	0.98
	ν_{23}	0.367	0.417	12.1	0.448	18.1	7.37
	α_{11} (10^{-6}/°C)	−0.712	−0.698	2.00	−0.685	3.94	1.86
	α_{22}, α_{33} (10^{-6}/°C)	12.1	11.6	4.91	11.6	4.17	0.71

Table 5. Comparisons of G_{23} for square and hexagonal unit cells to test transverse isotropy.

	Square cell (MPa)			Hexagonal cell (MPa)		
	G_{23}	$E_{23}/2(1+\nu_{23})$	% Error	G_{23}	$E_{23}/2(1+\nu_{23})$	% Error
Glass/epoxy	4.62	7.74	67.5	5.83	5.91	1.41
Graphite/epoxy	3.40	4.06	19.3	3.72	3.74	0.56

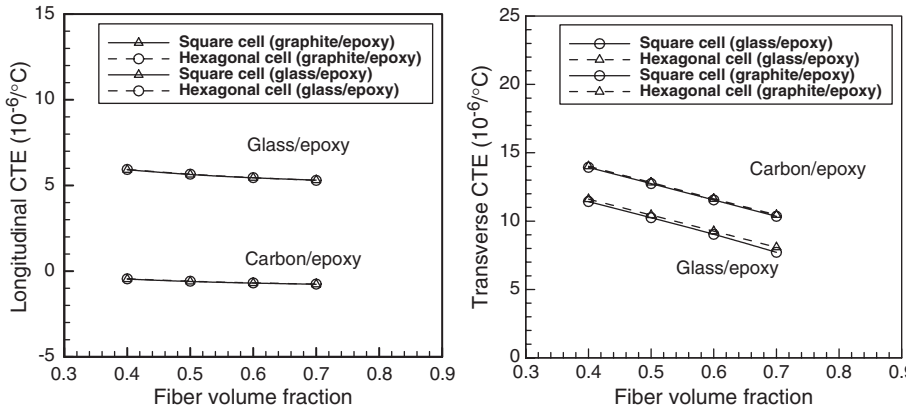

Figure 5. *Longitudinal and transverse CTE with various fiber volume fractions for glass/epoxy and graphite/epoxy laminates at $T = 50$ K.*

As shown in Table 5, the difference in the shear moduli calculated from the two methods is small for the hexagonal unit cell. Hence, the hexagonal unit cell model can be considered as more realistic for fiber-reinforced composites [2]. Also, the micromechanics method provides better results for lamina properties compared to empirical formulas.

EFFECTS OF FIBER VOLUME FRACTION

The effect of fiber volume fraction on the thermal coefficients of graphite/epoxy composite was analyzed using the micromechanics method. Figure 5 shows the variation of longitudinal and transverse thermal coefficients as a function of fiber volume fraction for glass/epoxy and graphite/epoxy composites at cryogenic temperature. The CTEs estimated using both square and hexagonal unit cells are very close. It should be noted that the graphite fiber has a negative thermal coefficient, and also the product of thermal coefficient α and Young's modulus (αE) is almost equal for the fiber and matrix. Hence the longitudinal thermal coefficients are negligibly small and they change sign as the fiber volume fraction is varied. At about 40% fiber volume fraction, the longitudinal thermal coefficient is almost equal to zero. The transverse thermal coefficient also reduces due to increase in fiber volume fraction because of the reduction in the effect of matrix material. The results show that the micromechanics method will be useful in developing a new composite material system for various applications by changing the combination of the constituent materials.

PREDICTION OF STRESSES AT MICROSCOPIC LEVEL

The micromechanics method was extended to estimate the microstresses of the graphite/epoxy composite laminate under combined thermal and external loads. The procedure used to obtain the relation between macro- and microstresses is described in the algorithm shown in Figure 6. Six independent sets of unit strains are applied to the unit cell boundary as explained in the previous section and microstresses are calculated in each element corresponding to the unit strain states. The temperature in the unit cell was also made equal to the temperature of the structure. The individual microstresses are multiplied by laminate strains in each layer calculated using the laminate theory [13].

The microstresses obtained by superposition are used to calculate the maximum and minimum stresses in each finite element in the unit cell model. The failure of the laminate can be predicted by using the maximum stress criterion for the fiber and matrix phases. The maximum stress criterion is reasonable as the fiber and matrix are expected to behave in a brittle manner at cryogenic temperature. The tensile strength of graphite fibers is taken as 1725 MPa and that of epoxy at cryogenic temperature is $\approx$100 MPa.

The graphite/epoxy composite laminates (IM7/977-3) with various stacking sequence (Specimen A: $[0]_s$; Specimen B: $[0/\overline{90}]_s$ and Specimen C: $[0/45/\overline{90}]_s$) were subjected to thermal stresses at cryogenic temperatures by using the FE-based micromechanics method. The thickness for each layer of the specimens is 0.07 mm. For the various laminated specimens, the longitudinal and transverse strains at the laminate level at cryogenic temperature ($\Delta T = -405$ K) were calculated using the laminate theory and they are presented in Table 6. The microlevel stresses were obtained by the superposition principle as described above. In the case of plane stress normal to the laminate plane, the strain in the thickness direction can be calculated by:

$$\varepsilon_3 = \frac{-C_{31}(\varepsilon_1 - \alpha_1 \Delta T) - C_{32}(\varepsilon_2 - \alpha_2 \Delta T)}{C_{33}} + \alpha_3 \Delta T \tag{5}$$

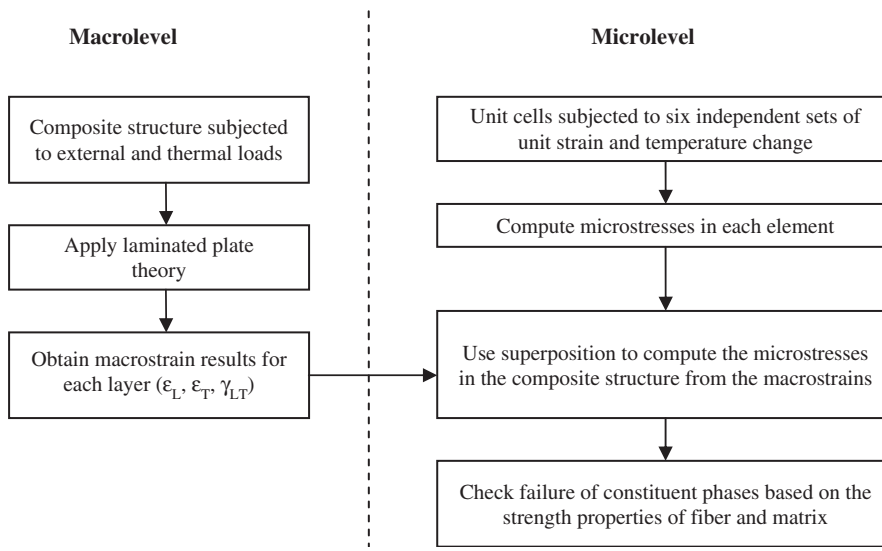

Figure 6. *Flow chart of algorithm used to predict the failure due to microstresses.*

Table 6. Macrostrains in different laminates due to thermal loads ($\Delta T = -405$ K). The subscript z denotes the thickness direction.

Sample	θ	ε_L (10^{-3})	ε_T (10^{-3})	ε_Z (10^{-3})	γ_{LT} (10^{-3})	γ_{LZ} (10^{-3})	γ_{TZ} (10^{-3})
A	0	0.277	−4.71	−4.71	0	0	0
B	0	0.0476	−0.382	−6.59	0	0	0
	90	−0.382	0.0476	−6.63	0	0	0
C	0	−0.130	−0.648	−6.406	1.410	0	0
	45	0.316	−1.094	−6.369	−0.518	0	0
	90	−0.648	−0.130	−6.449	−1.410	0	0

Table 7. Maximum principal stresses in the fiber and matrix phases in the unit cell of various graphite/epoxy laminates.

		Macroanalysis			Microanalysis							
					Square cell				Hexagonal cell			
		LPT			Fiber (MPa)		Matrix (MPa)		Fiber (MPa)		Matrix (MPa)	
Sample	θ	σ_L	σ_T	γ_{LT}	σ_1	σ_2	σ_1	σ_2	σ_1	σ_2	σ_1	σ_2
A	0	0	0	0	1.78	−36.9	39.4	−20.7	3.29	−33.8	41.3	−10.1
B	0	−24.9	46.4	0	54.3	−104	63.4	−35.5	51.2	−91.0	63.4	−21.8
	90	−92.9	49.9	0	59.0	−217	65.4	−36.3	55.2	−204	66.6	−22.9
C	0	−54.3	43.1	7.76	50.8	−155	69.2	−34.2	47.7	−147	68.4	−21.4
	45	16.2	39.5	−2.85	45.3	−33.5	61.3	−33.4	43.3	−23.4	61.3	−19.7
	90	−136	47.3	−7.76	55.9	−291	71.4	−35.4	52.2	−283	71.1	−22.7

Table 8. Percentage difference in results for principal stresses in the unit cell of various graphite/epoxy laminates.

		Fiber (MPa)		Matrix (MPa)	
Specimen	θ	σ_1 (%)	σ_2 (%)	σ_1 (%)	σ_2 (%)
A	0	84.7	−8.56	4.76	−51.2
B	0	−5.60	−12.1	−0.10	−38.5
	90	−6.33	−5.99	1.87	−37.0
C	0	−6.16	−4.92	−1.19	−37.5
	45	−4.57	−30.1	0.03	−41.2
	90	−6.61	−2.85	−0.39	−36.1

The macromechanical or structural analysis also provides stresses in each ply of the composite. These stresses can be expressed in the corresponding principal material coordinate system as shown in Table 7. The microstresses in the fiber and matrix phases are estimated using the micromechanics methods, and the principal stresses σ_1 and σ_2 are calculated based on the microstress results as shown in Table 7. The difference in principal stresses calculated using the square and hexagonal cells are presented in Table 8.

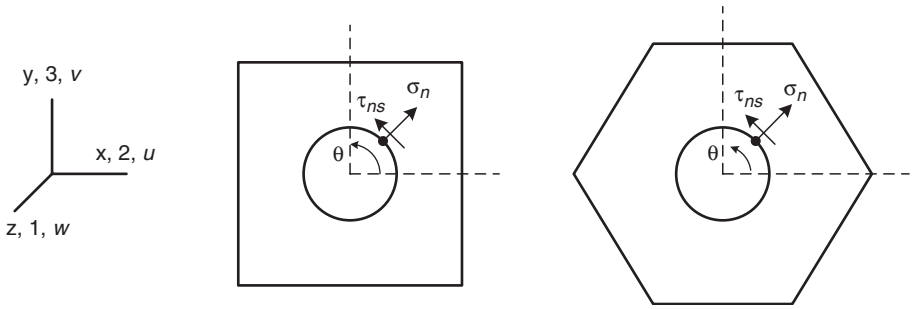

Figure 7. *Normal and shear stresses at the interface of fiber and matrix of square and hexagonal unit cells.*

The results for principal (micro) stresses σ_1 and σ_2 in the fiber and matrix phases are shown in Table 7. For the unidirectional laminate (Sample A), the laminate macrostresses calculated using the laminate theory is zero since the laminate undergoes free thermal contraction. However, the stresses at microscale are generated because of contraction between the fiber and the matrix. The difference in principal stresses calculated using the square and hexagonal cells are shown in Table 8. The maximum principal stress is relatively consistent for both square and hexagonal unit cells, but the minimum principal stress in the matrix is reduced by ≈40%. In the case of unidirectional laminate (Sample A), the stresses in the fiber are very small compared to the matrix stresses.

The results from the FE simulation can be used to compute the normal and shear stresses at the fiber–matrix interface in the unit cell. The normal and tangential stress components were calculated using the transformation matrix given in Equation (6).

$$\begin{bmatrix} \sigma_n \\ \sigma_s \\ \tau_{ns} \end{bmatrix} = \begin{bmatrix} \cos^2\theta & \sin^2\theta & 2\sin\theta\cos\theta \\ \sin^2\theta & \cos^2\theta & -2\sin\theta\cos\theta \\ -\sin\theta\cos\theta & \sin\theta\cos\theta & \cos^2\theta - \sin^2\theta \end{bmatrix} \begin{bmatrix} \sigma_x \\ \sigma_y \\ \tau_{xy} \end{bmatrix} \tag{6}$$

where θ is the angle measured from the x-axis as shown in Figure 7.

The normal and shear stresses around the periphery of the fiber are investigated when the uniaxial laminate is subjected at the cryogenic temperatures $\Delta T = -405\,\mathrm{K}$ without external loads. To compare the results for both unit cells, the interfacial stresses are plotted for the half region of the model ($90^\circ < \theta < 270^\circ$). The angle is measured from the horizontal axis of the model. From the results shown in Figure 8, one can see that the absolute values of interfacial normal and shear stresses are lower for the hexagonal unit cell. This means that the interfacial fracture between fiber and matrix is less likely to occur in a hexagonal unit cell than in a square unit cell.

In real composite, fiber distribution is closer to the hexagonal pattern, and hence the interfacial stresses will be less.

APPLICATION TO THE LIQUID HYDROGEN COMPOSITE TANK

The micromechanics method is used to predict the failure of the LH2 composite tank due to combined thermal and external loads. The LH2 composite tank is made of a

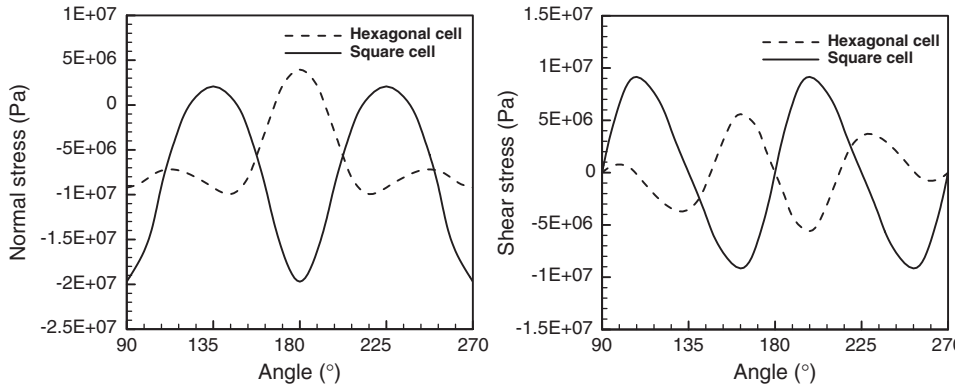

Figure 8. *Interfacial normal and shear stresses of uniaxial graphite/epoxy laminate system at* $\Delta T = -405\,K$.

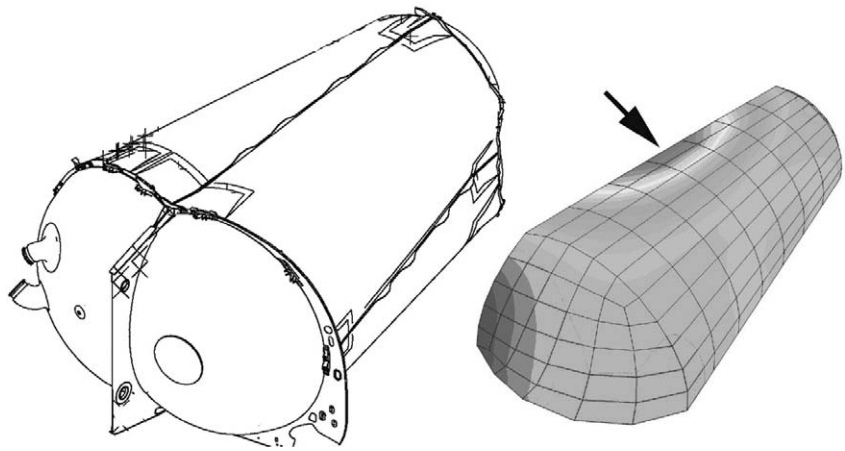

Figure 9. *Maximum principal stress distribution in the LH2 graphite/epoxy composite tank. Tank pressure = 10 kPa and temperature = 50 K (*$\Delta T = -405\,K$*). The arrow indicates where the peak stress occurs.*

honeycomb composite sandwich structure [1]. The inner face sheet is a 13-ply, IM7/977-2 laminate (0.066 in. thick) with the stacking sequence $[45/90_3/-45/0_3/-45/90_3/45]_T$. The outer face sheet is a 7-ply, IM7/977-2 laminate (0.034 in. thick) with the stacking sequence $[65/0/-65/90/-65/0/65]_T$. The material properties used for the IM7/977-2 laminates are estimated in Table 2. The honeycomb core is Korex 3/16–3.0 (1.5 in. thick). The elastic constants of the core are $E_1 = E_2 = 4.14\,\text{MPa}$, $E_3 = 137.9\,\text{MPa}$, $G_{12} = 4.14\,\text{MPa}$, $G_{13} = 74.5\,\text{MPa}$, $G_{23} = 15.9\,\text{MPa}$, $v_{12} = 0.25$, $v_{13} = v_{23} = 0.02$. The thermal expansion of the honeycomb core is assumed to be zero.

The LH2 composite tank is subjected to appropriate boundary conditions in the ABAQUS® FE model to simulate the situation at which it failed during proof test [1]. The actual LH2 composite tank was modeled using eight-node solid elements (see Figure 9). The quarter model of the composite tank has 137 elements with 75 integration points in the thickness direction. The layup configuration of the composite laminates is specified in the layered solid elements. The IM7/997-2 laminate properties used for the macromodel are given in Table 4.

The macrolevel analysis was performed to predict the microstress at the location where the peak stress occurs when the composite tank is subjected to internal pressure at cryogenic temperature. The analysis investigated two cases. In the first case, the tank was exposed to cryogenic temperature without internal pressure. In the second case, an internal pressure was applied in addition to the cryogenic temperature. The displacement contours shown in Figure 9 correspond to a pressure of 10 kPa and $\Delta T = -405$ K. The location denoted by the arrow in Figure 9 was selected for further investigation of failure due to microstresses. The macrolevel strains and curvatures in the longitudinal and transverse fiber directions were computed using the FE analysis (Tables 9 and 10). The microstresses

Table 9. Laminate macrostrains used to obtain the microstresses in the inner and outer facesheets of the sandwich composite at T = 50 K without internal pressure.

Layer	θ	ε_L (10^{-3})	ε_T (10^{-3})	ε_Z (10^{-3})	γ_{LT} (10^{-3})	γ_{LZ} (10^{-3})	γ_{TZ} (10^{-3})
Inner facesheet	45	−0.149	−0.227	−5.43	−0.299	0.512	−0.0831
	90	−0.0386	−0.338	−5.43	0.0773	0.422	0.302
	−45	−0.226	−0.150	−5.43	0.299	−0.0898	−0.510
	0	−0.338	−0.0380	−5.43	−0.0748	0.296	−0.425
	−45	−0.224	−0.151	−5.43	0.300	−0.0965	−0.508
	90	−0.0374	−0.337	−5.43	0.0723	0.428	0.289
	45	−0.152	−0.222	−5.43	−0.300	0.506	−0.103
Core	–	−0.337	−0.0367	−5.43	−0.0697	0.283	−0.431
Outer facesheet	65	−0.0899	−0.203	−5.51	−0.298	0.543	−0.452
	0	−0.296	0.00423	−5.51	0.106	−0.182	−0.684
	−65	−0.00858	−0.283	−5.51	0.162	−0.698	−0.123
	90	0.00447	−0.296	−5.51	−0.107	0.686	−0.185
	−65	−0.00792	−0.283	−5.51	0.161	−0.701	−0.121
	0	−0.296	0.00470	−5.51	0.108	−0.188	−0.687
	65	−0.0904	−0.0200	−5.51	−0.300	0.544	−0.463

Table 10. Laminate macrostrains used to obtain the microstresses in the inner and outer facesheets of the sandwich composite subjected to a pressure of 10 kPa at T = 50 K.

Layer	θ	ε_L (10^{-3})	ε_T (10^{-3})	ε_Z (10^{-3})	γ_{LT} (10^{-3})	γ_{LZ} (10^{-3})	γ_{TZ} (10^{-3})
Inner facesheet	45	−0.147	0.419	−5.90	−0.731	3.11	−3.69
	90	0.501	−0.230	−5.90	−0.563	4.81	−0.407
	−45	0.412	−0.144	−5.90	0.732	−3.67	−3.13
	0	−0.233	0.500	−5.90	0.553	−0.371	−4.81
	−45	0.405	−0.141	−5.89	0.734	−3.64	−3.16
	90	0.498	−0.236	−5.89	−0.543	4.81	−0.335
	45	−0.138	0.398	−5.89	−0.735	3.18	−3.62
Core	–	−0.238	0.497	−5.89	0.534	−0.299	−4.81
Outer facesheet	65	0.303	−0.366	−5.57	−0.622	5.30	0.118
	0	−0.485	0.422	−5.57	−0.115	2.36	−4.75
	−65	0.214	−0.280	−5.57	0.770	−3.31	−4.15
	90	0.421	−0.487	−5.56	0.119	4.75	2.37
	−65	0.212	−0.280	−5.56	0.774	−3.30	−4.17
	0	−0.489	0.421	−5.56	−0.122	2.39	−4.75
	65	0.306	−0.375	−5.56	−0.618	5.32	0.165

Table 11. Maximum and minimum principal stresses in the fiber and matrix phases in the inner and outer facesheets.

		Without tank pressure at $T = 50$ K				Tank pressure = 10 kPa at $T = 50$ K			
		Fiber (MPa)		Matrix (MPa)		Fiber (MPa)		Matrix (MPa)	
Layer	θ	σ_1	σ_2	σ_1	σ_2	σ_1	σ_2	σ_1	σ_2
Inner facesheet	45	58.8	−138	70.9	−2.71	77.8	−167	101	−21.2
	90	57.8	−107	69.3	−2.47	121	−33.5	93.2	−27.2
	−45	59.6	−157	71.0	−2.49	92.5	−37.1	96.4	−23.0
	0	60.6	−185	71.3	−2.73	79.0	−162	90.0	−14.1
	−45	59.6	−156	71.0	−2.50	90.8	−38.1	96.4	−22.8
	90	57.8	−107	69.3	−2.50	121	−33.7	92.9	−27.1
	45	58.8	−139	70.9	−2.74	77.5	−166	101	−21.4
Core	–	–	–	–	–	–	–	–	–
Outer facesheet	65	59.1	−123	71.3	−3.79	84.8	−78.0	93.1	−27.5
	0	61.1	−175	71.7	−3.74	80.8	−242	99.3	−16.2
	−65	58.2	−101	70.4	−3.99	74.7	−76.8	96.9	−19.0
	90	58.1	−97.5	70.3	−3.87	100	−45.7	96.2	−25.2
	−65	58.2	−101	70.4	−4.00	74.7	−77.3	97.0	−19.0
	0	61.1	−175	71.7	−3.75	80.8	−244	99.5	−16.3
	65	59.1	−123	71.4	−3.82	85.5	−77.7	93.0	−27.6

in the inner and outer facesheets were calculated using the superposition method described in the previous section.

The results of the maximum and minimum principal stresses in the fiber and matrix phases in each layer of the laminate are shown in Table 11. When the cryogenic temperature is applied to the composite tank without tank pressure, the maximum principal stress in the matrix phase (70 MPa) is below its strength (100 MPa). The result indicates that microstresses in the matrix phases, although very high, are not large enough to initiate microcracks. However, when the tank pressure increases and reaches 10 kPa, the microstress in the matrix in the inner facesheet exceeds the tensile strength indicating the possibility of microcrack development.

CONCLUSIONS

The LH2 composite tank proposed for space vehicles is exposed to extreme thermal and external loads. A finite element (FE)-based micromechanics method has been developed to predict the temperature-dependent thermomechanical properties of fiber composites such as graphite/epoxy. The unit cell was modeled using periodic boundary conditions. Temperature-dependent elastic constants and CTE of the matrix material were used in the FE analysis. The micromechanics method yields detailed microstress distribution in the fiber, matrix, and the interface between the fiber and the matrix. These microstresses can be used to predict microcracking of the composite at various temperatures with or without external loads. The method was used to analyze the stresses in the LH2 composite tank. The stresses in the matrix phase seem to exceed the tensile strength of the matrix material indicating that microcracking is a possibility. However, matrix strength measured at cryogenic temperatures should be used for the accurate prediction of the formation of microcracks.

ACKNOWLEDGMENTS

The authors gratefully acknowledge the technical and financial support of the NASA Glenn Research Center (NAG3-2750) and the NASA Kennedy Space Center under the Hydrogen Research and Education program. Partial support was provided by the CUIP (URETI) Program sponsored by NASA under NCC3-994, managed by the NASA Glenn Research Center and Florida Space Grants Consortium.

REFERENCES

1. Marshall Space Flight Center (2000). *Final Report of the X-33 Liquid Hydrogen Tank Test Investigation Team*, Huntsville, Alabama.
2. Hashin, Z. (1983). Analysis of Composite Material – A Survey, *ASME J. Applied Mechanics*, **50**(3): 481–505.
3. Chen, C.H. and Cheng, S. (1967). Mechanical Properties of Fibre Reinforced Composites, *Journal of Composite Material*, **1**(1): 30–40.
4. Teply, J.L. and Dvorak, G.J. (1988). Bounds on Overall Instantaneous Properties of Elastic–Plastic Composites, *Journal Mechanics and Physics Solids*, **36**(1): 29–58.
5. Paley, M. and Aboudi, J. (1992). Micromechanical Analysis of Composites by the Generalized Cells Model, *Mechanics of Materials*, **14**(2): 127–139.
6. Nedele, M.R. and Wisnom, M.R. (1994). Finite Element Micromechanical Modeling of a Unidirectional Composite Subject to Axial Shear Loading, *Composites*, **25**(4): 263–272.
7. Marrey, R.V. and Sankar, B.V. (1995). Micromechanical Models for Textile Structural Composites, NASA Contractor Report, 198229.
8. Sankar, B.V. and Marrey, R.V. (1997). Analytical Method for Micromechanics of Textile Composites, *Composites Science and Technology*, **57**(6): 703–713.
9. Marrey, R.V. and Sankar, B.V. (1997). A Micromechanical Model for Textile Composite Plates, *Journal of Composite Materials*, **31**(12): 1187–1213.
10. Li, S. (1999). On the Unit Cell for Micromechanical Analysis of Fibre-reinforced Composites, *Proceedings of the Royal Society of London, Series A*, **455**: 815–838.
11. Usami, S., Ejima, H., Suzuki, T. and Asano, K. (1999). Cryogenic Small-flaw and Creep Deformation of Epoxy Resin, *Cryogenics*, **39**: 729–738.
12. Bechel, V. and Kim, R. (2004). Damage Trends in Cryogenically Cycled Carbon/Polymer Composites, *Composites Science and Technology*, **64**: 1773–1784.
13. Agarwal, B. and Broutman, L. (1990). *Analysis and Performance of Fiber Composites*, **2nd edn**, pp. 13–53, John Wiley & Sons, Inc., New York, NY.
14. Elseifi, M. (1998). A New Scheme for the Optimum Design of Stiffened Composite Panels with Geometric Imperfections, PhD Dissertation, Virginia Polytechnic Institute and State University, Blacksburg, VA.